

Article

# Novel Copper Oxide Bio-Nanocrystals to Target Outer Membrane Lectin of Vancomycin-Resistant *Enterococcus faecium* (VREfm): In Silico, Bioavailability, Antimicrobial, and Anticancer Potential

Mahmoud Kandeel <sup>1,2,\*</sup> , Mohamed Sharaf <sup>3,4,\*</sup> , Arshad Mahdi Hamad <sup>5</sup> , Ahmad O. Babalghith <sup>6</sup> , Mohnad Abdalla <sup>7,\*</sup> , Muhammad Arif <sup>4</sup>, Reem Binsuwaidan <sup>8</sup> , Nashwah G. M. Attallah <sup>9</sup>, Hossam Aladl Aladl Aladl <sup>10</sup>, Samy Selim <sup>11</sup>  and Mariusz Jaremko <sup>12</sup>

- <sup>1</sup> Department of Biomedical Sciences, College of Veterinary Medicine, King Faisal University, Al-Hofuf 31982, Saudi Arabia
  - <sup>2</sup> Department of Pharmacology, Faculty of Veterinary Medicine, Kafrelshikh University, Kafrelshikh 33516, Egypt
  - <sup>3</sup> Department of Biochemistry, Faculty of Agriculture, AL-Azhar University, Nasr City, Cairo 11651, Egypt
  - <sup>4</sup> Department of Biochemistry and Molecular Biology, College of Marine Life Sciences, Ocean University of China, Qingdao 266003, China
  - <sup>5</sup> Department of Biology, College of Science, Tikrit University, Tikrit 34001, Iraq
  - <sup>6</sup> Medical Genetics Department, College of Medicine, Umm Al-Qura University, Mecca 24382, Saudi Arabia
  - <sup>7</sup> Pediatric Research Institute, Children's Hospital Affiliated to Shandong University, Jinan 250022, China
  - <sup>8</sup> Department of Pharmaceutical Sciences, College of Pharmacy, Princess Nourah Bint Abdulrahman University, Riyadh 11671, Saudi Arabia
  - <sup>9</sup> Egyptian Drug Authority (EDA) Previously NODCAR, Giza 12513, Egypt
  - <sup>10</sup> Department of Internal Medicine, Faculty of Medicine, AL-Azhar University, Nasr City, Cairo 11651, Egypt
  - <sup>11</sup> Department of Clinical Laboratory Sciences, College of Applied Medical Sciences, Jouf University, Sakaka 72388, Saudi Arabia
  - <sup>12</sup> Smart-Health Initiative and Red Sea Research Center, Division of Biological and Environmental Sciences and Engineering, King Abdullah University of Science and Technology, Thuwal 23955-6900, Saudi Arabia
- \* Correspondence: mkandeel@kfu.edu.sa (M.K.); mohamedkamel@azhar.edu.eg (M.S.); mohnadabdalla200@gmail.com (M.A.)



**Citation:** Kandeel, M.; Sharaf, M.; Hamad, A.M.; O. Babalghith, A.; Abdalla, M.; Arif, M.; Binsuwaidan, R.; G. M. Attallah, N.; Aladl Aladl Aladl, H.; Selim, S.; et al. Novel Copper Oxide Bio-Nanocrystals to Target Outer Membrane Lectin of Vancomycin-Resistant *Enterococcus faecium* (VREfm): In Silico, Bioavailability, Antimicrobial, and Anticancer Potential. *Molecules* **2022**, *27*, 7957. <https://doi.org/10.3390/molecules27227957>

Academic Editor: Louis Pergaud Sandjo

Received: 11 October 2022  
Accepted: 9 November 2022  
Published: 17 November 2022

**Publisher's Note:** MDPI stays neutral with regard to jurisdictional claims in published maps and institutional affiliations.



**Copyright:** © 2022 by the authors. Licensee MDPI, Basel, Switzerland. This article is an open access article distributed under the terms and conditions of the Creative Commons Attribution (CC BY) license (<https://creativecommons.org/licenses/by/4.0/>).

**Abstract:** In present study, we used *Olea europaea* leaf extract to biosynthesize in situ Copper Oxide nanocrystals (*CuO @OVLe NCs*) with powerful antibacterial and anti-cancer capabilities. Physicochemical analyses, such as UV/Vis, FTIR, XRD, EDX, SEM, and TEM, were applied to characterize *CuO @OVLe NCs*. The UV/Vis spectrum demonstrated a strong peak at 345 nm. Furthermore, FTIR, XRD, and EDX validated the coating operation's contact with colloidal *CuO @OVLe NCs*. According to TEM and SEM analyses, *CuO @OVLe NCs* exhibited a spherical shape and uniform distribution of size with aggregation, for an average size of ~75 nm. The nanoparticles demonstrated a considerable antibacterial effect against *E. faecium* bacterial growth, as well as an increased inhibition rate in a dose-dependent manner on the MCF-7, PC3, and HpeG2 cancer cell lines and a decreased inhibition rate on WRL-68. Molecular docking and MD simulation were used to demonstrate the high binding affinity of a ligand (Oleuropein) toward the lectin receptor complex of the outer membrane to vancomycin-resistant *E. faecium* (VREfm) via amino acids (Leu 195, Thr 288, His 165, and Ser 196). Hence, our results expand the accessibility of *OVLe's* bioactive components as a promising natural source for the manufacture of physiologically active components and the creation of green biosynthesis of metal nanocrystals.

**Keywords:** nanocrystal; *Olea europaea*; *Enterococcus faecium*; green biosynthesis; antimicrobial; anti-cancer; molecular docking; molecular dynamic simulation

## 1. Introduction

Antibiotics have saved many lives over the last 100 years, and experts once believed that humans might eradicate illnesses caused by bacteria. On the other hand, antibiotic misuse has steadily built resistance, resulting in the eradication of antibiotics after decades of usage and the emergence of several multidrug-resistant microorganism strains that are insensitive to conventional antibacterial strategies, such as *E. faecium* [1]. Drug resistance is a significant danger linked with microbial infections, leading to treatment failure. Currently, various health organizations throughout the globe are warning that multidrug-resistant microorganisms are a serious hazard since they risk thousands of lives and have an unquantifiable cost [2–6].

Vancomycin-resistant *Enterococcus faecium* (VREfm) is a gram-positive aggressive pathogen that often infects the human and animal oral cavity, digestive tract, and genital tract. VREfm has no negative implications for the host in a healthy individual. Unfortunately, in immunocompromised people, the pathogen can induce life-threatening diseases [7,8].

Antibiotic overuse in recent years has accelerated the growth of antibiotic-resistant bacterial strains (particularly vancomycin-resistant strains), resulting in their predominance in human and animal germs [9]. In recent years, managing infections induced by VREfm has become extremely challenging due to the frequency of multidrug-resistant *E. faecium* strains, particularly vancomycin-resistant strains, generating severe concerns among healthcare professionals [10]. A thick layer of peptidoglycan typically surrounds gram-positive microorganisms, which suggests that in *E. faecalis*, peptidoglycan alteration by secondary cell wall polymers is crucial for evading complement identification [11]. *E. faecalis* secondary cell wall polymers are required for tolerance to complement stimulation by coupling with lectin [12].

As a result, new treatment alternatives that are less successful at selecting for resistance, such as plant-derived phenolic chemicals, are necessary. Nano-antibiotics have broad antibacterial efficacy against bacteria, protozoa, and fungi. Metallic nanoparticles have received significant attention since metals have inherent antibacterial properties and display antimicrobial effect regardless of microbe drug sensitivity profiles. Furthermore, nanoparticles may increase the efficacy of currently available antimicrobial drugs [13].

Plants have medical significance because they include chemical substances that perform a particular physiological function in the human body. Phenolic compounds, alkaloids, tannins, and flavonoids are the major significant bioactive plant substrates [14]. Because of their polyphenol antioxidant and anti-inflammatory properties, certain phytochemicals can greatly lower antibacterial and cancer risk. Preclinical research suggests that phytochemicals can help prevent breast, colorectal, and other cancers [15].

Metal nanoparticles are synthesised using plant materials such as leaves, roots, latex, seeds, and stems [16,17]. Techniques for producing nanoparticles using naturally available reagents such as plant extracts may be appealing for nanotechnology. Furthermore, they can be utilised to minimise the toxicity of a medicinal medicine [18].

The olive tree's (*Olea europaea*, Oleaceae) leaves (Figure 1A,B) are widely employed in traditional herbal therapies to avoid and treat a wide range of diseases, including antimicrobial, diabetes, cardiovascular disease, cancer, and several health problems, because they contain several critical antioxidant and phenolic components to avoid oxidative damage [19–21]. Oleuropein, tyrosol, and hydroxytyrosol, in addition to caffeic acid and ligstroside, are antioxidant compounds found in the olive tree that have been linked to the prevention of several illnesses [22]. Oleuropein, a naturally occurring compound of the secoiridoid group, is the primary active ingredient in olive leaf and its extract. Several investigations have shown that oleuropein possesses a range of pharmaceutical and health-promoting properties, including antispasmodic, immune-stimulating, cardioprotective, hypotensive, anti-inflammatory, antioxidant, anti-cancer, and antithrombotic properties [20,23].



**Figure 1.** (A) *Olea europaea* L. folium (Oleaceae) leaves; (B) Botanical Voucher Specimen, MOBOT, Tropicos.org (<http://www.tropicos.org/Image/100000992>, accessed on: 1 April 2022).

In present study, we modified the method of preparation of Copper Oxide NPs using olive leaf extract at room temperature (25–27 °C) in order to preserve the active compounds of the plant extract and to avoid breaking them at high temperatures during preparation as in other methods mentioned previously (100 °C) [24], which increases their effectiveness. As a result, the purpose of this research was to examine the size-controlled compounds to biosynthesize in situ nanoscale Copper Bio-nanocrystals Oxide (CuO NCs) used *Olea europaea* leaf extract and surface functionalization using in situ oxidation–precipitation techniques, together with the exploration of the antimicrobial, and anticancer efficiency. Moreover, this is the first publication to identify the phytochemicals substrate (oleuropein) antimicrobial properties of vancomycin-resistant *Enterococcus faecium* (VRE $f_m$ ) via greatly improving their interactions with lectin outer membrane protein.

## 2. Results and Discussion

### 2.1. Role of Phyto-Reductants and Capping of OVLe Agents for Tailoring and Characterization of OVLe@CuO NCs

According to earlier investigations, the oleuropein exists in high concentrations compared to other phenolic components as observed by the HPLC chromatogram of olive leaf extract [25,26]. Oleuropein, a highly unstable molecule that quickly breaks down into the more polarizable hydroxytyrosol (C<sub>8</sub>H<sub>10</sub>O<sub>3</sub>) in organic solvents, may have played a role in the capping action CuO-NS underwent in the current work to modify high-energy planes (atoms). During the synthesis of NS, it may concurrently function as a phyto-reducing and phyto-capping agent [27].

#### 2.1.1. UV-Vis Absorption Spectroscopy Analysis

As the olive leaf extract, the absorption peak gets more sharpness and blue shift was observed from 400 to 458 nm (Figure 2A). The copper salt, which is reduced by the ions to create nanoparticles, forms complexes with the phytochemicals in the extracts. Therefore, we employed UV-Vis spectroscopy in the 200–1100 nm range to examine the color change in the produced Solutions. Due to the CuO @OVLe NCs 'core electrons' inter-band transition, Figure 2B shows a notable peak at 345 nm. These findings resembled Aziz et al. [28]. For the synthesis of CuO @OVLe NCs, Mahmoud et al. 2021 also employed orange peel and mint leaf extract, and they discovered their absorption peak at 325 nm [29].

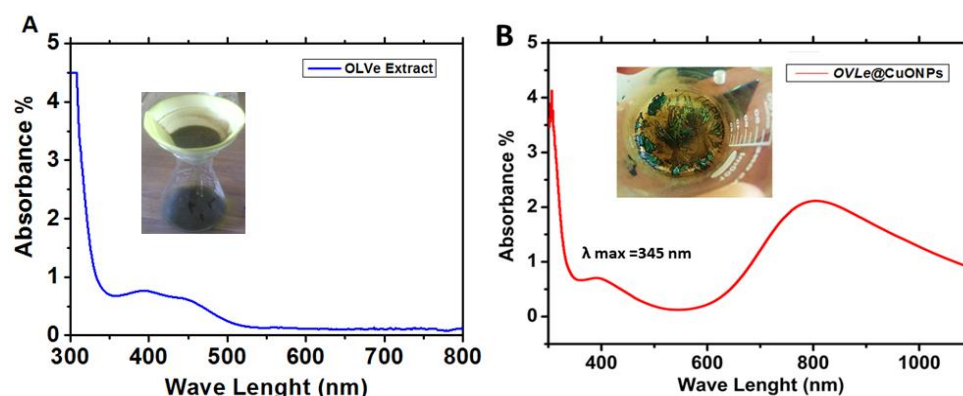


Figure 2. UV-Vis absorption spectra: (A) Olive leaf extract (OVLe), (B)  $\text{CuO} @\text{OVLe}$  NCs.

### 2.1.2. FTIR Analysis

As a consequence, we noticed that the FTIR vibration varied depending on the functional groups. These groups have a distinctive absorption in the IR region that causes the compound's energy bonds to stretch and curve more in the peaks. The FTIR spectra revealed the presence of different functional groups. The IR bands (Figure 3A) observed at  $3408.72$  and  $1740.33 \text{ cm}^{-1}$  in dried olive leaf were characteristic of the O-H and C=O stretching modes for the OH and C=O groups, possibly of oleuropein, apigenin-7-glucoside, and/or luteolin-7-glucoside. The very strong band at  $1080.23 \text{ cm}^{-1}$  could be assigned to the C-OH vibrations of the protein in the olive leaf. These results are close to those mentioned by Khalil et al. [30]. In addition, the surface chemical coordinates and chemical composition of the  $\text{CuO} @\text{OVLe}$  NCs were examined by FTIR. The functional groups in the  $\text{CuO} @\text{OVLe}$  NCs were identified using the peaks shown in Figure 3B. The C-O, O-H, and H-H bond order frequencies are seen in the vibration modes between  $2500$  and  $4000 \text{ cm}^{-1}$  [27]. The identified Cu-O peak locations were at  $592$ ,  $607$ , and  $665 \text{ cm}^{-1}$ , whereas  $453 \text{ cm}^{-1}$  was discovered for the Cu-O stretching bond frequency. The findings related to Cu-O are consistent with earlier studies [31,32].

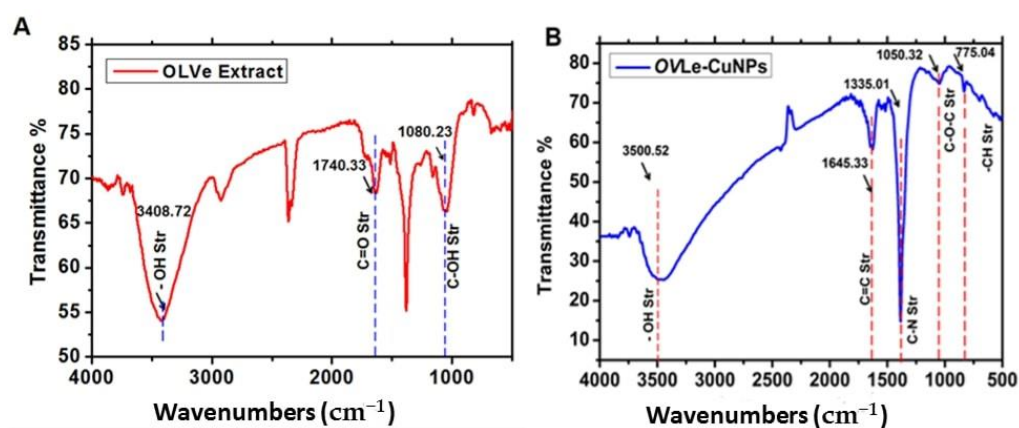


Figure 3. FTIR spectra: (A) Olive leaf extract (OVLe), (B)  $\text{CuO} @\text{OVLe}$  NCs.

### 2.1.3. XRD Analysis

XRD patterns were used to determine the materials' structure and phase purity, as illustrated in Figure 4. Overall,  $2\theta$  values of  $67.79^\circ$  (533),  $64.84^\circ$  (202),  $55.23^\circ$  (201),  $54.50^\circ$  (112),  $52.50^\circ$  (200),  $51.52^\circ$  (103),  $46.33^\circ$  (110),  $39.29^\circ$  (102),  $36.33^\circ$  (101),  $29.01^\circ$  (002), and  $26.3^\circ$  (100) degrees, the strong diffraction peaks were seen. When compared to the information from stander values (JCPDS card No. 48-1548), the diffraction peaks of XRD are extremely well matched with those found by Siddiqui et al. [33]. The produced  $\text{CuO} @\text{OVLe}$  NCs were confirmed by each reflection peak. This pattern adheres to the International Centre for Diffraction Data's normative peaks. In addition, the wide breadth of the diffraction bands

in X-ray diffraction patterns indicated tiny particle sizes. These results were expected based on previous studies by Padil et al. [34].

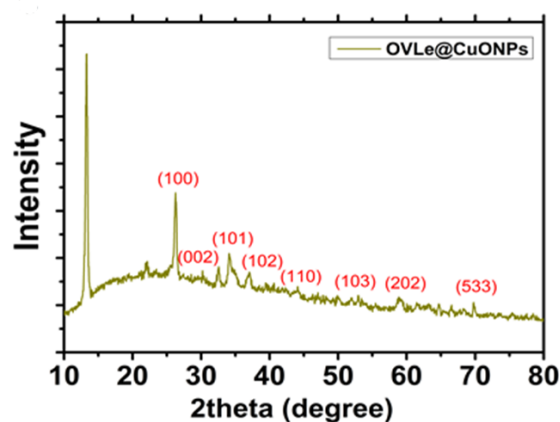


Figure 4. XRD of  $\text{CuO} @\text{OVLe}$  NCs.

#### 2.1.4. Surface Morphology

SEM analysis was used to determine the  $\text{CuO} @\text{OVLe}$  NCs' size, shape, and surface morphology. Figure 5A,B and Figure 6A, respectively, exhibit TEM and SEM images. According to certain structural properties, the synthesised products had spherical and crystalline structures and diameters of  $76.37 \pm 4.9$  nm. Overall, previous findings support the notion that producing CuO NCs using an aqueous leaf extract of *OVLe* is an efficient and environmentally benign method. The findings support numerous previous investigations, as shown in our current investigation [32]. Energy dispersive X-ray spectroscopy (EDX) was used to determine the elements that comprise the biogenic  $\text{CuO} @\text{OVLe}$  NCs. Figure 6B displays the results of an EDX investigation that identified copper (44.08%) and oxygen (55.92%). A high peak at 0.93 keV and a peak at 8.24 keV were also seen, both of which indicated the presence of copper (Cu), while a peak at 0.473 keV was linked to the presence of oxygen (O). Previous studies have shown that a number of EDX-discovered elements, including Si, Au, and Cl, act as capping agents for biogenic CuO NPs. The reactivity, surface area, rate of absorption into microbial cells, cell surface contact, protein binding, and other properties of NPs are determined by their size and shape [35], and these parameters are of prime importance for antimicrobial applications. These results indicate that the designed nanoparticles of formulations around  $\sim 75$  nm were small enough to satisfy the steric prerequisite for rapid diffusion through the bacteria's outer membrane. These results confirmed the successful biosynthesis of copper nanoparticles. It was also found that the bio coating shell process for CuO NPs did not affect the phase change of copper oxide.

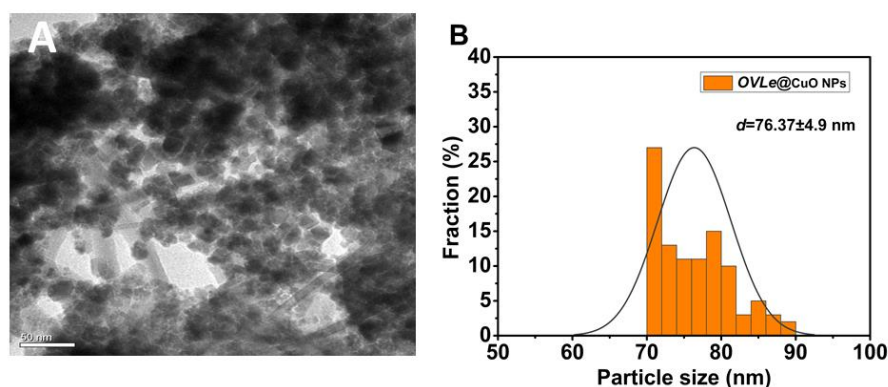
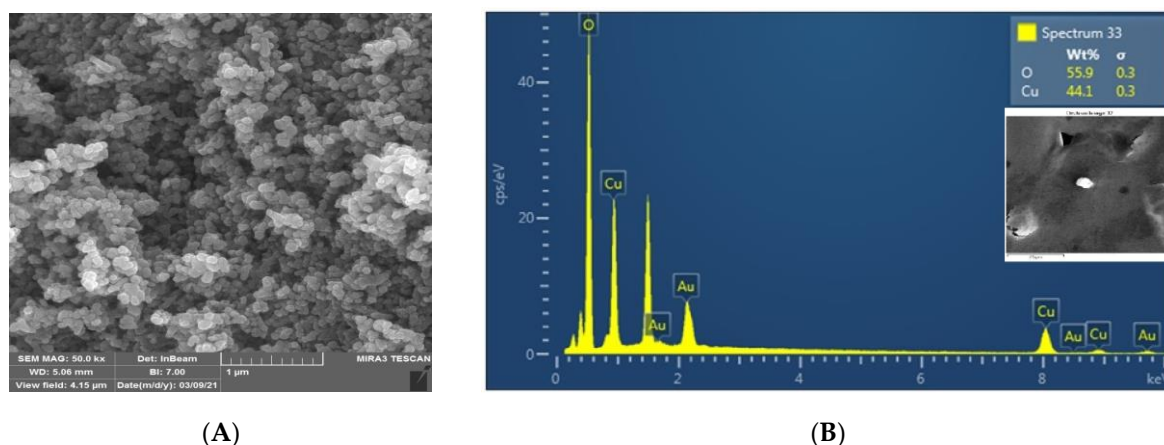


Figure 5. (A) Average particle size of prepared  $\text{CuO} @\text{OVLe}$  NCs evaluated utilising TEM (scale bar = 50 nm). (B) The size distribution of prepared  $\text{CuO} @\text{OVLe}$  NCs data is shown as the mean  $\pm$  SD ( $n = 3$ ).



**Figure 6.** (A) The shape of synthesized  $\text{CuO} @\text{OVLe}$  NCs assessed utilising SEM (scale bar = 1  $\mu\text{m}$ ); (B) EDX profile.

## 2.2. Antibacterial Potential of $\text{CuO} @\text{OVLe}$ NCs

$\text{OVLe}$  and  $\text{CuO} @\text{OVLe}$  NCs suspensions at different concentrations were analysed for antibacterial activity against  $VREfm$  cultured on Muller-Hinton agar medium at 37 °C for 24 h using a disc diffusion assay. The ability of the antibacterial agent (NPs) to rupture the bacterial cells is shown in Table 1 and Figure 7.

**Table 1.** Zone of inhibition (mm) plate with diverse concentrations of  $\text{OVLe}$  and  $\text{CuO} @\text{OVLe}$  NCs.

VREfm Zone of Inhibition (mm)			
Treatment	Inhibition Zone	Treatment	Inhibition Zone
OLVe 10 mg/mL	5.7	$\text{CuO} @\text{OLVe}$ 10 mg/mL	11.07
OLVe 15 mg/mL	6	$\text{CuO} @\text{OLVe}$ 20 mg/mL	18.02
OLVe 20 mg/mL	6.3	$\text{CuO} @\text{OLVe}$ 30 mg/mL	22.06
OLVe 25 mg/mL	6.5	Negative Control (Tigecycline, 25 $\mu\text{g}/\text{mL}$ )	17.01
OLVe 30 mg/mL	7.2	Positive Control	NI

NI: No inhibition.

$\text{OVLe}$  showed mild inhibitory action, with a maximum zone of the inhibition region mainly depending on the concentration of 7.2 mm against  $VREfm$  for high concentrations of 30 mg/mL/disk (Figure 7A,B). No zone of inhibition was detected for the positive control ( $\text{DIH}_2\text{O}$ ) on the disk of  $VREfm$ . Tigecycline was determined as a negative control which recorded an inhibition zone diameter of 17.01 mm (Figure 7C–E). These results are in agreement with that of Latifa et al. [36], who found that the antibacterial efficiency of isolates produced resistance results of  $VREfm$  (zone diameter  $\leq 15$  mm) utilising the disk diffusion assay.

The quantitative evaluation of antibacterial  $\text{CuO} @\text{OVLe}$  NCs by diffusion in the pits was performed, and it was observed that the inhibition region mainly depended on the concentration. However, the  $VREfm$  strain exhibited the highest sensitivity to  $\text{CuO} @\text{OVLe}$  NCs at the concentrations of 30 mg/mL/disk and recorded inhibition zone diameters of 22.06 mm (Figure 7C,E), which may have been due to the divergent physio-chemical characteristics of  $\text{CuO} @\text{OVLe}$  NCs. In addition,  $\text{CuO} @\text{OVLe}$  NCs showed mild inhibitory action with a maximum zone of inhibition of 11.07 mm and 18.02 mm for  $\text{CuO} @\text{OVLe}$  NCs against  $VREfm$  for differential concentrations of 10 and 20 mg/mL/disk, respectively (Figure 7C–E). The multimode actions that green fabricated  $\text{CuO} @\text{OVLe}$  NCs caused the complete growth inhibition of all  $VREfm$  bacterial strains.

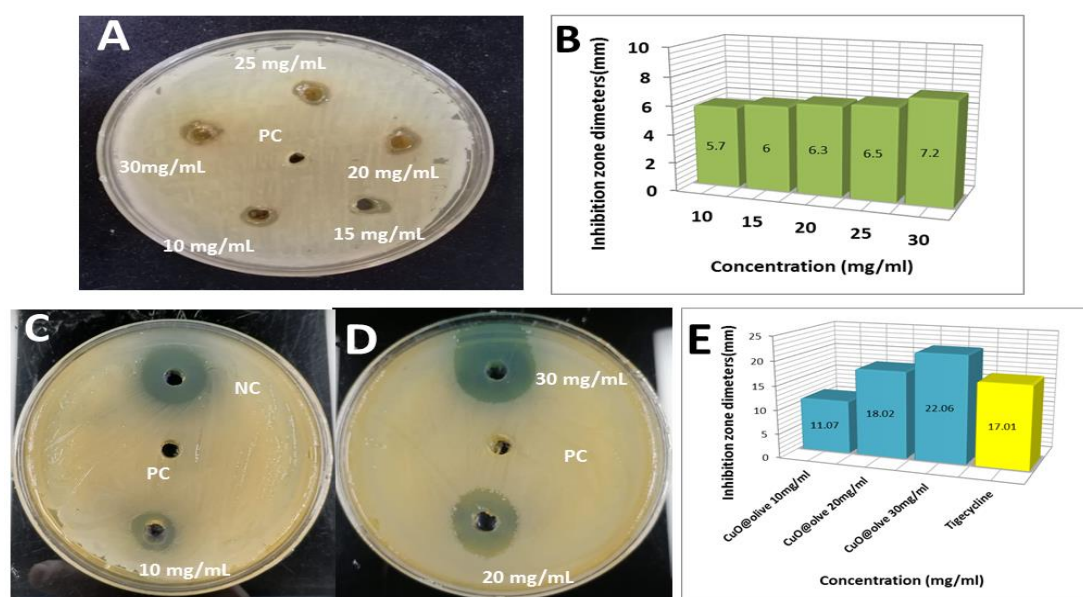


**Figure 7.** (A) Zone of inhibition (mm) plate with diverse concentrations 10, 15, 20, 25, and 30 mg/mL of OVLe; (B) *Enterococcus faecium* bacterial growth curve; (C,D) zone of inhibition (mm) plate with diverse concentrations 10, 20, and 30 mg/mL of CuO @OVLe NCs; (E) *Enterococcus faecium* bacterial growth curve.

Cu has shown varied inhibitory activity due to its various physio-chemical properties. Olive leaf extract phyto-reductants have also demonstrated modest inhibitory activities, and the bactericidal capabilities of olive plant extract are extensively documented in the literature [26,37]. The observed differential in the zone of inhibition across bacterial strains might be attributed to gram-negative pathogens having structural changes in their cell walls, such as the deposition of lipopolysaccharide material [38], the velocity of NS diffusion through the chemical properties, bacterial envelop, ionic discharge, binding activation energy, and surface charge attraction, which increases their pathogenicity [39]. Cu has a changeable oxidation state that alternates between  $\text{Cu}^+$  and  $\text{Cu}^{2+}$ , which can be attributed to the fact that most transition metals can include either 3d or 4s shells for electron shuffling [40]. When metal ions with varying oxidation states are exposed to the biological environment, they can cause deadly ROS. Even more reactive and heavily contributing to the production of ROS are metal ions from NPs. According to the theory in Figure 6, the antibacterial action in our investigation may also be closely related to the photoactivation of ROS by NPs on bacterial growth [41]. Furthermore, the cellular environment is affected by lethal ROS species ( $\text{OH}^-$ ,  ${}_{1}\text{O}_2^-$ , and  ${}^*\text{O}_2$ ), which increases oxidative stress. Direct genome destruction, ROS-induced mitochondrial damage, plasmid and cell protein denaturation, and partial or complete loss of cell wall permeability are mainly induced by the upregulation in oxidative stress [42].

### 2.3. Screening Cytotoxicity Study and Anti-Cancer of CuO @OVLe NCs

Both the normal cell line (WRL-68) and the cancer cell line (MCF-7, PC3, and HpeG2) were treated with concentrations ranging between 31.25 and 250  $\mu\text{g}/\text{mL}$  of CuO @OVLe NCs (Figure 8) for 24 h at a temperature of 37  $^\circ\text{C}$  at a rate of three replicates for each concentration. The control sample without treatment was used for comparison. The extent of the toxicological effect was also evaluated by extracting the percentage of the growth inhibition rate compared to the control (100% growth). The 3T3 Phototox software was used to estimate the  $\text{IC}_{50}$  of prepared samples in different cell lines using the absorbance values disclosed in the following capture of the red dye and the appropriate amounts of the CuO @OVLe NCs employed in the cytotoxicity studies. The highest quantities of CuO @OVLe NCs examined in this study showed minimal toxicity to the normal cell line WRL-68

and to cancer cells (PC3, HpeG2, and MCF-7) (Figure 8). They increased the inhibition rate in a dose-dependent manner of MCF-7 cells ( $IC_{50}$ , approximately 45.24  $\mu\text{g}/\text{mL}$ ), PC3 cells ( $IC_{50}$ , approximately 126.40  $\mu\text{g}/\text{mL}$ ), and HpeG2 cells ( $IC_{50}$ , approximately 58.74  $\mu\text{g}/\text{mL}$ ), and increased the cell viability and decreased the inhibition rate of WRL-68 at a high dose ( $IC_{50}$ , approximately 143.50  $\mu\text{g}/\text{mL}$ ). Biresaw and Taneja (2022) found approximately similar results when studying Copper nanoparticles with green synthesis derived from *Prunus nepalensis* phytochemicals [43]. Furthermore, CuNPs synthesized from different plant extracts, such as *Ficus religiosa* [44], indicated cytotoxic activities on breast (MCF-7) cancer cell lines and human liver carcinoma cells (HepG2) in a concentration-dependent manner, which was probably mediated through ROS generation and oxidative stress. Our findings may be due to the level of glycolipids and glycopeptides increasing significantly in the cell wall of cancer cells compared to normal cells, as these substances act as special receptors. The resulting Cu ion can interact large biomolecules such as enzymes, DNA, and RNA, inducing the oxidation process, and cause damage to the mitochondria [45]. In addition, green CuNPs nanoparticles affect the cancer cell, inhibiting the respiratory chain and stopping ATP synthesis [46]. Moreover, the effect on the cancerous line compared to the natural one, such as the MCF-7 cancer line and HepG2, was due to the selectivity to some metabolic properties that cancer cells possess and their absence in normal cells, such as their metabolic nature, the receptor shape on the surface of the cancer cells, and the affinity to bind to various compounds [47–49]. Further, it has been reported that green synthesized CuO NPs exhibit a low cytotoxic nature and genotoxic toward normal somatic cells compared to NPs produced by other chemical or physical approaches [50,51]. Doped or undoped CuO NPs engineered by different chemical techniques also demonstrated cytotoxicity to healthy cells [52].

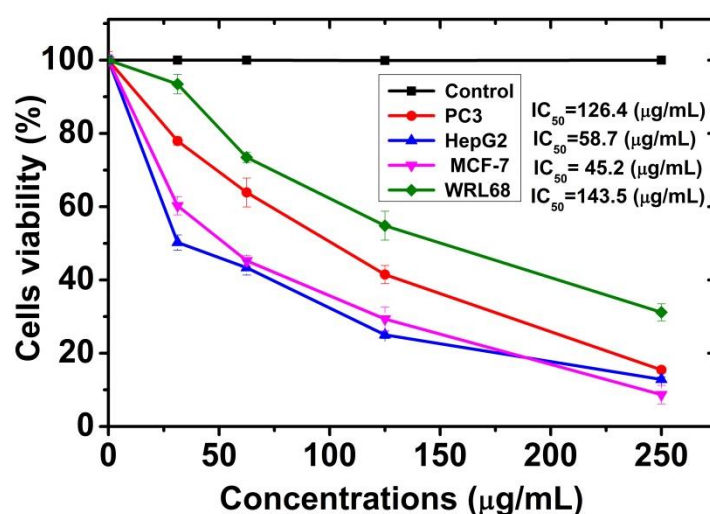


**Figure 8.** Viability of normal WRL68 cell and cancer cells (PC3, HepG2, and MCF-7), cells treated with different concentrations of CuO @OVLe NCs. Numerical data are described as the mean  $\pm$  SD ( $n = 3$ ).

#### 2.4. Molecular Docking and Interaction of Ligands with the Active Site of *Enterococcus faecium* Lectin

According to earlier investigations, oleuropein (ligand) abundance over other phenolic components was observed in the HPLC chromatogram of olive leaf extract [25,26]. This compound was further selected for molecular docking studies to gain further insight into the molecular working mechanism by which lectin-ligand (*EFLe*c–ligand) inhibits, as no published reports have described the protein-ligand structure. The result is shown in Figure 9.

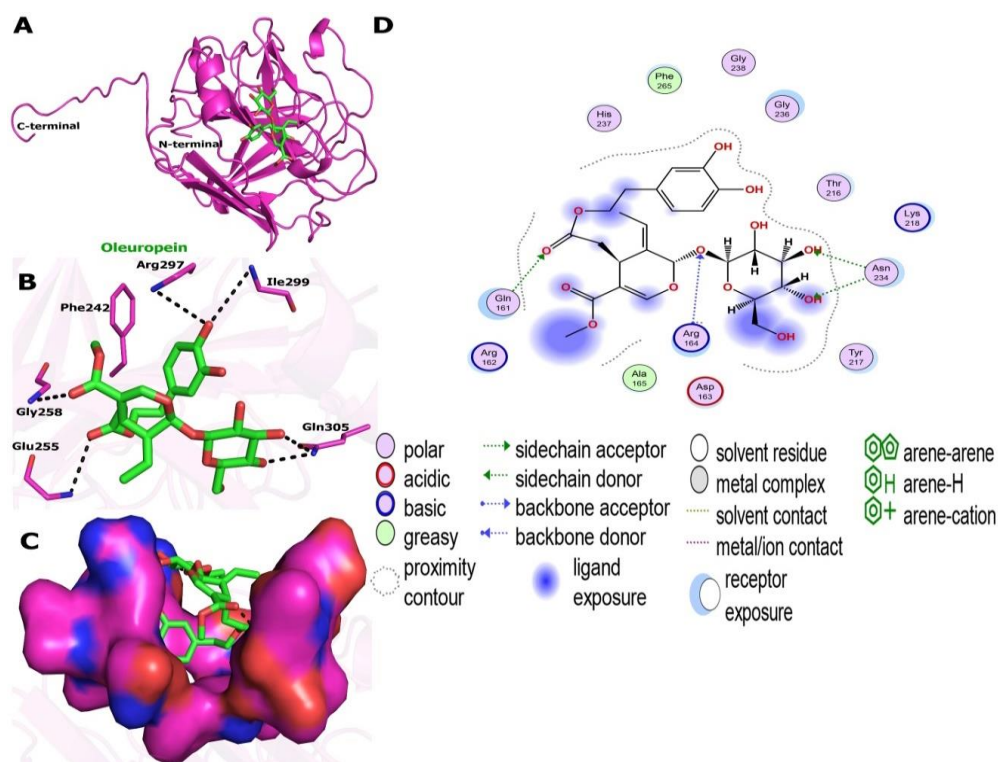


**Figure 9.** Molecular docking study of oleuropein toward the binding pocket of *EFLec*. (A) The surface representation of the active-site flap of *EFLec* with ligand, shown at the entrance of the binding pocket. (B) Amino acids involved in a hydrogen bond with oleuropein are shown as sticks. PyMol created these figures. Oleuropein (cyans), the crystal structure of *EFLec* (NCBI ID WP\_033741131.1) (greens), and oxygen atoms are presented in red, and nitrogen atoms are shown in blue and purple dashed lines assigned to the bonding interactions. (C) Electrostatic surface of *EFLec*. Positive charges are in blue, negative charges are in red, and neutral charges are in purple. (D) Van der Waals and alkyl interactions with the residues of the catalytic site that are crucial for inactivating the enzyme.

*Enterococcus faecium* lectin (NCBI ID WP 033741131.1) has 11 $\alpha$  helices and 7 $\beta$  strands. Auto lectin dock tools were used for molecular docking. Figure 9A shows *EFLec*–ligand binding modes as cartoons. Thr 244 (OH distance = 2.75), Gln305 (OH distance = 2.83), Gln305 (OH distance = 3.03), Gly245 (OH distance = 3.27), Gly258 (OH distance = 3.94), and Thr257 (OH distance = 2.82) formed hydrogen bonds (Table 1 and Figure 8B).

In the docked confirmation, the complete fitness and logarithm of lectin's free binding energy ( $\Delta G$ ) were  $-1220.23$  and  $-9.5$  kcal/mol, respectively. Ligand and *EFLec* docking scores were also observed. Figure 9B shows the results. The predicted *EFLec* and ligand models for in silico docking were credible. *EFLec* active site amino acids were both high and less conserved. The conserved amino acids had ligand-binding motifs. Dimer binding motifs and surface residues were identified. All residues were allowed. Electrostatic forces were considered in the in silico docking experiments. Phe242, Thr244, Lys246, Glu255, Arg297, Asp301, and Gln305 formed hydrogen bonds.

In addition to carbohydrates, the ligand can interact with hydrophobic molecules in dimeric or tetrameric lectin structures, such as Ala232, Try254, Leu302, and Ile299. Figure 8B shows stable ligand binding. These hydrophobic interactions may explain why lectin *Enterococcus faecium* increases and decreases ligand activity [43,53]. A lectin-resveratrol phenolic compound interaction occurred in ConM's hydrophobic cavity [54]. These results suggest that phenolic compounds extracted from plants, such as oleuropein, may be an alternative therapeutic tool to modify bacterial resistance. Half of the oleuropein locus was in the positive charge area during the in silico docking studies. Half was naturally electrostatic (Figure 9C). The results show that ligand interacted with *EFLec*'s

active site through hydrogen bonding and van der Waals alkyl interactions (Figure 9D). These interactions inhibited *EFLeC* activity. The ligand binded to the enzyme's active pocket and interacted with the guanosine-5'-diphosphate active sites. The ligand competed with the substrate and created protein-product complexes as a competitive inhibitor.

### 2.5. Interaction Analysis of Ligand with Target *EFLeC*

The ligand showed six interactions with the allosteric site residues of the target lectin protein. Six hydrogen bond interactions were observed, as shown in Table 2. The binding affinity energy (S-Score) of the allosteric site of the target protein was  $-9.5$  kcal/mol.

**Table 2.** Interaction analysis of ligand with target *EFLeC*.

Ligand	Receptor/Amino Acid	Interaction Distance	E (kcal/mol)
O7/17	OG1/Thr244	H-donor 2.75	-1.2
O4/19	NE2/Gln305	H-acceptor 2.83	-2.5
O3/21	NE2/Gln305	H-acceptor 3.03	-1.2
O10/27	CA/Gly245	H-acceptor 3.27	-1.1
O10/27	CA/Gly258	H-acceptor 3.49	-0.9
O11/42	OG1/Thr257	H-acceptor 2.82	-2.6

Figure 10A shows the bioavailability radar for a ligand with high activity potential; it meets all oral-use criteria (Table S1). The potent hits were physicochemical, pharmacokinetic, and drug-like (Bioavailability Source: 0.11, Ghose: NO, TPSA: 201.67 2, water solubility: 2.72 mg/mL soluble, BBB permeant: NO, P-gp substrate: NO, CYP isoform interacts: NO, oleuropein is water-soluble). Oleuropein does not cross the blood-brain barrier, does not interact with CYP450 enzymes, and is a P-gp substrate.

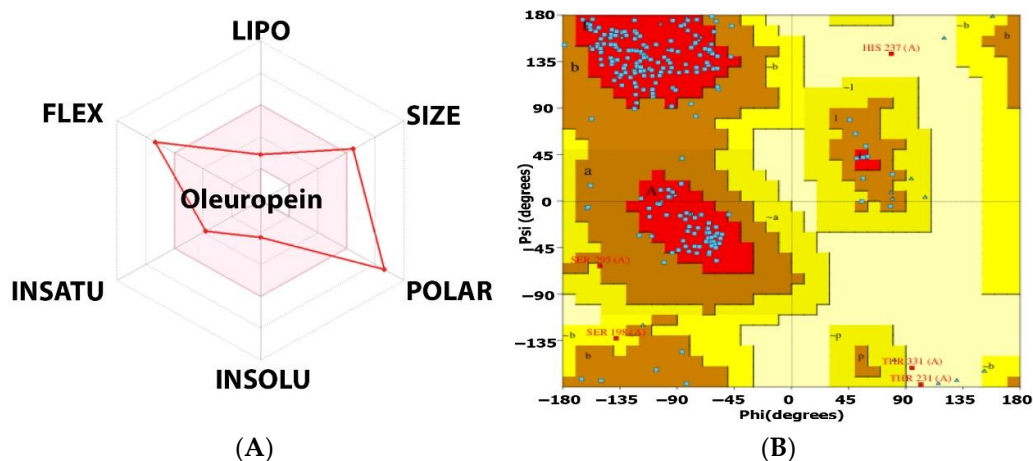


**Figure 10.** A three-dimensional interaction scheme of oleuropein with the catalytic site of *EFLeC*. (A) Bioavailability radar related to physicochemical properties of molecules (criteria: MW 540.51 g/mol, fraction Csp3: 0.52, TPSA < 201.67 Å<sup>2</sup>, molar refractivity: 127.28, instauration, flexibility: 0.54 < rotatable bonds < 7), and (B) Ramachandran plot for the predicted model of the docking of oleuropein.

Ramachandran plots were utilised to verify the results. Overall, 100% of the residues were in the allowed area, while none were in the disallowed area. G-factors indicate a stereochemical property's oddness. Below  $-1.0$ , the abnormality is high, and below  $-0.5$ , it is odd. G-factors for the main chain and dihedral angles were 0.5. According to the Ramachandran plot and G-factors, the 3D model's backbone dihedral angles, phi, and psi were within permissible limits of the Programmer PROCHECK, RMSD, and ProSA (Figure 10B).

## 2.6. Molecular Dynamic Simulations

The inhibition of *EFLec* by ligands was assessed using an MD simulation and multiple dynamic trajectories (RMSD and RMSF; Figure 11A,B). Figure 11A shows a protein's RMSD. Throughout the simulation, RMSD revealed the protein's structure. RMSD analysis showed that oscillations near the MD simulation's end were average thermal structures. Small and globular proteins, where MD simulation convergence is key, can tolerate 2.00–3.20 changes. RMSD should be a constant.

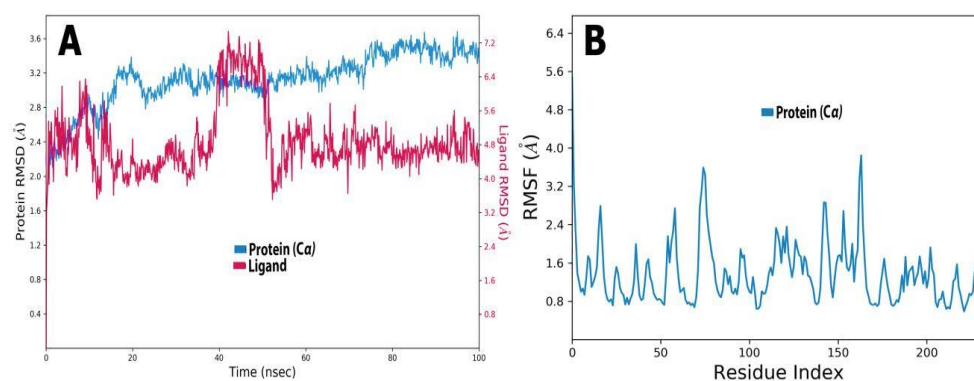


**Figure 11.** (A) RMSD plot obtained for oleuropein of the protein-ligand *EFLec* complexes. Protein  $\alpha$  and compound RMSD are shown in blue and red colour, respectively. (B) RMSF plot of the protein's backbone atoms during the 100 ns MD simulation. Protein  $\alpha$  RMSD is shown in blue.

A study of the RMSF profile of the *EFLec* protein bound with oleuropein revealed fluctuations in the urease sequence. The RMSF profile for *EFLec* protein showed 1–2 nm fluctuations. Our study found no change at the *EFLec*–oleuropein active site. Non-catalytic site mobility was much higher, ranging from 4 to 50 nm, but this was not significant for the current study, which focused on the active site of *EFLec* (Figure 11B).

## 2.7. Ligand Torsion Profile and Properties

Figure 12A,B show the ligand torsion histogram throughout the simulation trajectory (0.00 ns to 100.05 ns). In Figure 12A, the ligand 2D-structure with colour-coded RB, as well as radial and bar plots for each RB torsion, are shown. The dial (or radial) graphs show the simulation's torsion. The allosteric ligand was flexible, and the -OH side groups rotated along the simulated pathway. These data may reveal the ligand's conformational strain to bind to protein (Figure 12B).

Figure 12C shows the examined ligand properties: RMSD, radius gyration, solvent-accessible surface area, molecular surface area, and polar surface area (PSA). The RMSD balanced to 100 ns. The ligand's RMSD in reference conformation (time  $t = 0.00$ ) varied from 1.00 Å<sup>2</sup> to 2.00 Å<sup>2</sup>, and its balance was about 2.50 Å<sup>2</sup>.

Ligand length was measured in rGyr, or main inertia moment. According to the results, the rGyr showed ligand fluctuation until 40.00 ns of simulation, ranging from 4.20 Å<sup>2</sup> to 5.20 Å<sup>2</sup>, and attaining equilibrium at 4.60 Å<sup>2</sup>.

The MolSA ligand was altered throughout the simulation. The ligand's MolSA varied from 420 Å<sup>2</sup> to 570 Å<sup>2</sup> and achieved equilibrium at 450 Å<sup>2</sup>.

The SASA of the *EFLec*-ligand complex fluctuated until 40.00 ns during the MD simulation, then stabilized 170 Å<sup>2</sup> to 380 Å<sup>2</sup> and attained equilibrium at 280 Å<sup>2</sup>.

The PSA values of the ligand ranged from 240 Å<sup>2</sup> to 360 Å<sup>2</sup> until 40.00 ns and attained equilibrium at 320 Å<sup>2</sup>. Finally, all ligand attributes changed over the start or simulation period but found equilibrium at the conclusion. These results indicate that the ligand possessed a stable interaction to the active site of the protein.

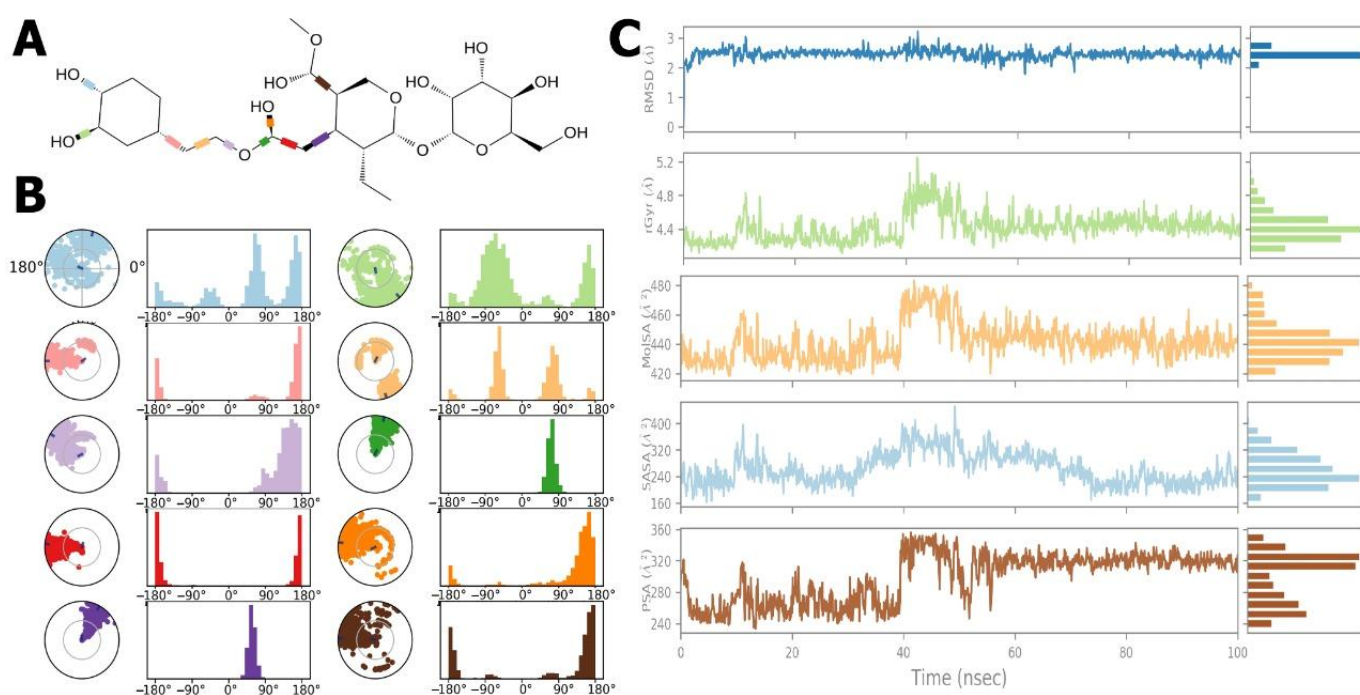


**Figure 12.** Ligand torsion profile: (A) torsion and flexibility, (B) ligand torsion angles, and (C) ligand (oleuropein) property trajectory of the ligand-*EFLec* complex. The ligand properties fluctuated during the beginning or intermediate simulation periods, but gradually returned to equilibrium during 100 ns of simulation, indicating that ligand was stable at the active site of the protein.

H-bonds impact drug selectivity, metabolism, and adsorption in drug design. MD simulations boosted *EFLec*-ligand H-bond interactions while reducing the average total energy (Figure 13A,B). In silico analysis indicated that oleuropein's docking conformation might build an H-bond with *EFLec*'s binding pocket residues. Ionic interactions occurred when two oppositely charged atoms came within 3.7 of one other, and no H-bond occurred. Phe242, Lys246, Glu255, Arg294, and Arg297 demonstrated little ligand-ionic interactions. Lau210, Ala232, Phe242, Ile299, Tyr252, and Leu302 reacted with aromatic or aliphatic ligand groups (Figure 13A). The water bridges represent H-bonded protein-ligand interactions mediated by water. Most major interacting amino acids (Ile230, Phe242, Thr244, Pro245, Lys246, Tyr253, Ser253, Gly254, Glu255, Arg294, Ser296, Ile298, Asp301, Leu302, Glu305, and Arg297) interacted through H-bonding and extremely efficient protein-ligand complex temporal interactions (100 ns simulation) (Figure 13B).

The ligand-receptor interaction histogram describes the protein-ligand interactions (Figure 13C). Figure 13C shows the number of protein-ligand interactions along the pathway. Above the trajectory curve series, interactions increased from 0.00 to 5.00. The role of amino acids in 100 ns MD simulations was studied. The orange scale below the graphic highlights residues that made several ligand contacts in a particular trajectory frame. The *EFLec* receptor-ligand complex showed deep orange bands (Phe242, Thr244, Lys246, Tyr252, Gly254, Glu255, Arg297, Ile298, and ArgAsp301 orange rows), suggesting that the amino acids exhibited excellent interactions with the ligand in almost all orientations (geometry). These results agree with our histogram findings.

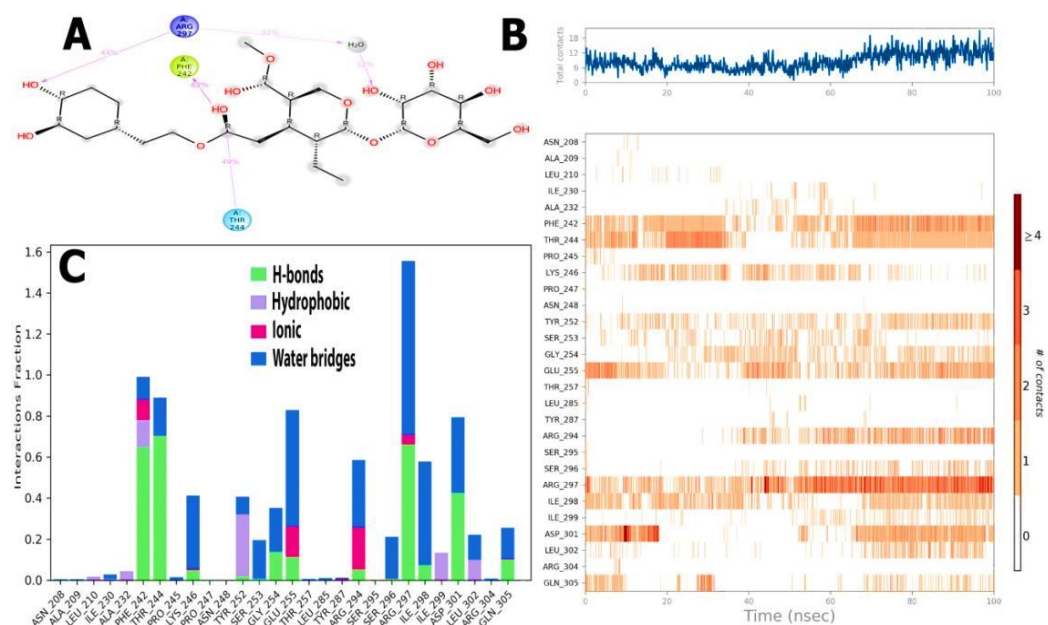


**Figure 13.** (A) Backbone RMSD values of the C $\alpha$  atoms of the protein, (B) RMSF of the backbone atoms, (C) snapshots of the docking pose of oleuropein and the total H-bond intensity at various time intervals in the 20 ns complex MD simulations with *EFLec*.

### 3. Materials and Methods

#### 3.1. Collection Samples

Fresh *Olea europaea* leaves were harvested with some branches from the Horticulture Department Medicinal Plants Garden of the Faculty of Agriculture, AL-Azhar University, Cairo, Egypt. The leaves were removed from the stems and cleaned by distilled water to remove residual dirt debris several times, then the leaves were left in the open air for a quarter of an hour in the shade until they dried.

#### 3.2. Preparation of Olive Leaf Extract

Distilled water was used to extract phytochemicals from fresh leaves according to [55], with some minor modifications. In brief, the leaves were crushed and coarsely ground into a powder. The *OVLe* extraction was performed by soaking 1 g of the powder in 100 mL of deionized water. The solution was thoroughly mixed for 72 h and heated at 40 °C with continuous stirring using a magnetic stirrer. Then, the solution was left to cool down to room temperature. The colour of the extract was light greenish yellow. Finally, the extraction was filtered using (Whatman No.1) filter paper and kept at −20 °C in a volumetric glass vial to be employed in the green synthesis of copper nanoparticles.

#### 3.3. Biosynthesis of CuO @OVLe NCs

*CuO @OVLe NCs* were synthesized using copper chloride as described by [56]. In brief, 40 mL of copper chloride (2 mM) was taken in an Erlenmeyer flask then mixed for almost 2 h. The *OVLe* mixture (1 mL) was subjected to the copper chloride solution under vigorous shaking (200 rpm) for 4 h at ambient temperature (25–27 °C) to permit the development of *CuO @OVLe NCs*. The solution soon became turbid and brown. To eliminate any contaminants or absorbed ions, the solution was centrifuged for 10 min at 12,000 rpm and rinsed with dH<sub>2</sub>O. Finally, the resultant was dried in the oven for 48 h at 45–50 °C with fan air.

#### 3.4. Characterizations of CuO @OVLe NCs

Using the UV-Visible spectra, the optical characteristics of nanocrystal powder derived from the quantity of green production of copper oxide nanoparticles (*CuO @OVLe NCs*)

were determined. The diluted samples were evaluated on a spectrophotometer (Varian Cary-100 Konc, Varian, Australia), at 230 V/50 Hz, at wavelengths of 200–800 nm. X-ray diffraction (XRD) patterns of the prepared *CuO @OVLe NCs* were recorded using the Rigaku D/Max-III C X-ray diffractometer (Rigaku Int. Corp. Tokyo, Japan). It formed with a CuK $\alpha$  radiation set (20 mA and 40 kV) diffractions at a scanning rate of 20/min between 2 and 500 at ambient temperature. The FT-IR analysis was recorded for the prepared samples to investigate the functional groups using the JASCO FT-IR 4100 spectrometer (Hachioji, Tokyo, Japan) as potassium bromide (KBr) discs. A high-pressure disc was loaded and assessed with a resolution of 4.0 cm<sup>-1</sup> at a wavelength of 400–4000 cm<sup>-1</sup> [57].

### 3.5. Surface Morphology

Scanning electron microscopy (SEM) was used to image the optimised samples (JSM 6390<sup>®</sup>, JEOL DATUM Ltd., Tokyo, Japan). A drop of *CuO @OVLe NCs* dried for 5 min on the aluminium mesh below a mercury lamp coater to a thickness of 400 Å. For transmission electron microscopy (TEM), measurements were assessed by TEM (TOPCON002B; Tokyo, Japan). Equipment was used to examine the silver nanoparticle. By simply placing a small amount of the sample on the mesh and blotting away any surplus solution with blotting paper, thin films of silver nanoparticles were formed on a carbon-coated copper grid [58].

### 3.6. Culture of the Microorganism

Muller-Hinton agar medium was used to cultivate *Enterococcus faecium* for 24 h at 37 °C. Using UV-Vis spectroscopy (Varian Cary-100 Konc, Varian, Australia), the colonisation was collected and assembled in HBSS (pH 6.0) to 0.06 at 600 nm (OD<sub>600</sub>), which amounted to ~10<sup>6</sup> (CFU) mL<sup>-1</sup>. It was then utilised in the examinations.

### 3.7. Antimicrobial Activity

The well diffusion method was used by producing three replications according to the method [59]. The bacterial suspension was prepared and dispersed throughout the medium on the medium of Muller-Hinton agar by means of a swab and afterward left for 5 min to dry. Then, 5 holes were made. Considering one of the pits as a conventional control, 50 µL of *OVLe* leaf extract (5, 10, 20, and 30 mg/mL) and *CuO @OVLe NCs* were attached in each pit at consecutive concentrations (10, 20, and 30 mg/mL), then put in the incubator for 24 h at 37 °C. DIH<sub>2</sub>O was employed as negative control, and tigecycline as a positive control. The inhibitory efficacy *CuO @OVLe NCs* against the bacteria was measured by the diameter of the inhibition region in millimetres using a standard ruler [60,61]. The outcomes are presented as mean ± standard deviation (SD).

### 3.8. Cell Lines

The normal liver cell line WRL 68 Cell as well as the cancer cell lines MCF-7, PC3 and HpeG2 were obtained from the University of Malaya College of Medicine Department of Pharmacy Center for Natural Product Research and Drug in Malaysia, Discovery Department of Pharmacology, Faculty Of Medicine, University of Malaya Kuala Lumpur Malaysia. Cancer cells were sustained and developed, and tests were conducted on them at the Biotechnology Research Center at Al-Nahrain University. All investigations were carried out using sterile deionized water (Milli-Q water).

### 3.9. Cytotoxicity Activity

The cytotoxic evaluation of the cancer cell lines MCF-7, PC3, and HpeG2 and normal liver cell line WRL-68 were evaluated with MTT. Following incubation, the medium from the wells was drained, and MTT solution (6 mg/mL) was added. The cells were placed in 60 µL of dimethylsulfoxide (DMSO), which was dissolved by rinsing the medium. The

absorbance spectra of the specimens were identified using a microplate reader with a wavelength of 595 nm [62].

$$\% \text{ Cell viability} = (A_{\text{test}} - A_{\text{blank}}) / (A_{\text{control}} - A_{\text{blank}}) \quad (1)$$

where A means optical density, test means the cells subjected to the *CuO @OVLe NCs* sample, control means the control sample, and blank means the wells without normal and cancer cells [63–65].

### 3.10. Molecular Docking

Structures in three dimensions of the citrus bioflavonoid oleuropein were downloaded from PubChem (ID 10621) [66]. They were docked onto the structure of the *Enterococcus faecium* lectin (NCBI ID WP 033741131.1) [67] using AutoDock Vina [68,69]. The docking pocket was determined using the default setting of AutoDock Vena. The utilised docking Grid Size was (Center X: 35.4 Y: 117.4 Z: 10.9), and dimensions (Angstrom) X: 41.8 Y: 42.9 Z: 45.3. The ligands were thought to be flexible, hence a ligand-specific torsion tree was created. Aside from that, the structure of protein was assumed rigid, and a grid covering the entire protein structure was established to represent the search area for possible interaction sites. As a result, pre-calculated maps for the ligands were constructed, including separate maps for each atom in the ligand and incorporating desolvation together with electrostatic potentials. Furthermore, the Auto Grid technique was used to calculate the interaction energy of a ligand conformation by adding the contributions of atoms from a given element at any position in the grid near the stiff receptor. The docking results that passed a criterion of  $\Delta G < -8.28$  kcal/mol were sorted based on the predicted interaction energy after scanning the complete protein structure search space [70–75]. As a result, the highest-ranking ligand posture was picked as a projected interaction model. ADME profiling of oleuropein was performed according to [76].

### 3.11. Interaction of Oleuropein into the Active Pocket of *ECLec*

A technique for two-dimensional interaction of oleuropein together with the catalytic site of *ECLec* was designed by Discovery Studio 2019 software [77], Pymol software was used to generate the conservation score homology model and the electrostatic surface [78,79], pdbsum generated the Ramachandran plot for the anticipated model [80,81].

### 3.12. Molecular Dynamics Simulations (MD Simulations)

MD simulations were performed on the protein-ligand compounds utilising the Schrodinger Maestro package [82]. MD simulations of the *ECLec*-oleuropein docked complexes were carried out to illustrate the effectiveness of hesperidin in inhibiting lectin. The Lec topology file was created in the Gromacs software. The molecular dynamic simulation with a 2 fs time step use the charmm36 forcefield with TIP3P water model [83]. The pressure and temperature were measured using the Parrinello-Rahman algorithm and Nose-Hoover temperature coupling at 310 K and 1 bar, respectively. The simulations were run for 100 ns in the NPT collection. Per 20 ps, the trajectories are preserved. The visualization of trajectories was performed using VMD. The MD runs were accomplished on an Intel core I7 processor with 32 GB RAM, running a Linux operating system (Ubuntu v14.041) on a Thunderobot laptop.

### 3.13. Statistical Analysis

The results of statistical investigation are displayed as mean  $\pm$  SEM. In contrast, one-way ANOVA determined statistical examination of data collected experimentally (\*  $p < 0.05$ , \*\*  $p < 0.01$ , and \*\*\*  $p < 0.001$ ) were regarded as significant differences when associated with the control. Graph Pad Prism 5.0 Version for Windows was used to evaluate statistical results (San Diego, CA, USA) [84,85].

#### 4. Conclusions

Copper Bio-nanocrystals Oxide was successfully prepared using *Olea europaea* leaf extract as antimicrobial and anticancer reducing agents. When compared to chemical approaches, the applied method has various advantages, including ease of preparation, cost-effectiveness, and safety. The green synthesis process may be used to produce various metal oxide nanoparticles. UV/Vis, FTIR, XRD, EDX, SEM, and TEM were used to characterise *OVLe@CuO* NCs. The maximum UV/Vis wavelength was detected at 345 nm. The existence of colloidal *OVLe@CuO* NCs was verified by FTIR, XRD, and EDX. The *OVLe@CuO* NCs were found to be spherical and uniform in size, with an average size of 75 nm, as indicated by TEM and SEM. The nanoparticles inhibited the growth of VREfm and exhibited a potent anti-breast cancer activity. Further, a molecular docking simulation was used to demonstrate the catalytic activity of a ligand (oleuropein) with a lectin receptor complex of the outer membrane to VREfm with water solubility. The ligand exhibited P-gp substrate qualities according to the physicochemical, pharmacokinetic, and drug-likeness features of powerful hits. The MD simulations of these protein-ligand complexes demonstrated conformational alterations during ligand interaction with active site residues, as indicated by a comprehensive investigation of the dynamic trajectories and H-bond profiles throughout 100 ns of simulation. Taken together, our findings open new avenues for exploring safe and effective anti-*E. faecium* from *Olea europaea* leaf extract and developing novel pharmacologically active compounds by the green biosynthesis of metal nanocrystals.

**Supplementary Materials:** The following supporting information can be downloaded at: <https://www.mdpi.com/article/10.3390/molecules27227957/s1>, Table S1: ADME predicted calculations of Oleuropein.

**Author Contributions:** Conceptualization, M.K., M.S., A.M.H., M.A. (Mohnad Abdalla), M.A. (Muhammad Arif) and M.J.; methodology, M.K., M.S., A.M.H., A.O.B., M.A. (Mohnad Abdalla), M.A. (Mohnad Abdalla) and H.A.A.A.; software, M.S., A.O.B., R.B., N.G.M.A., H.A.A.A. and M.J.; validation, M.S., A.M.H., M.A. (Mohnad Abdalla), M.A. (Muhammad Arif), R.B., S.S. and M.J.; formal analysis, M.S., A.M.H., A.O.B., R.B., N.G.M.A., H.A.A.A. and S.S.; investigation, M.K., M.S., A.M.H., M.A. (Mohnad Abdalla), M.A. (Muhammad Arif), H.A.A.A. and M.J.; resources, M.K., M.S., A.O.B., R.B., H.A.A.A. and M.J.; data curation, M.S.; writing—original draft preparation, M.K., M.S., A.M.H., M.A. (Mohnad Abdalla) and M.A. (Muhammad Arif); writing—review and editing, M.K., M.S., A.M.H., A.O.B., M.A. (Mohnad Abdalla), M.A. (Muhammad Arif), R.B., N.G.M.A., H.A.A.A., S.S. and M.J.; visualization, M.S., A.M.H., A.O.B., M.A. (Mohnad Abdalla), M.A. (Muhammad Arif), N.G.M.A. and H.A.A.A.; supervision, M.K., M.S., A.M.H., M.A. (Mohnad Abdalla), M.A. (Muhammad Arif) and M.J.; project administration, M.K. and M.S.; funding acquisition, M.K., R.B. and M.J. All authors have read and agreed to the published version of the manuscript.

**Funding:** This research was funded by Princess Nourah bint Abdulrahman University Researchers Supporting Project number (PNURSP2022R65), Princess Nourah bint Abdulrahman University, Riyadh, Saudi Arabia. This work was also supported by the Deanship of Scientific Research, Vice Presidency for Graduate Studies and Scientific Research, King Faisal University, Saudi Arabia (Project# GRANT1889). The research was also supported by the Faculty of Medicine, Al-Azhar University, Egypt.

**Institutional Review Board Statement:** Not applicable.

**Informed Consent Statement:** Not applicable.

**Data Availability Statement:** Not applicable.

**Acknowledgments:** The authors extend their appreciation to Princess Nourah bint Abdulrahman University for funding this work through Researchers Supporting Project number (PNURSP2022R304), Princess Nourah bint Abdulrahman University, Riyadh, Saudi Arabia. The authors also extend their appreciation to the Deanship of Scientific Research, Vice Presidency for Graduate Studies and Scientific Research, King Faisal University, Saudi Arabia (Project# GRANT1889).

**Conflicts of Interest:** The authors declare no conflict of interest.

**Sample Availability:** Samples of the nanoparticles are available from the authors.

## References

1. Langdon, A.; Crook, N.; Dantas, G. The effects of antibiotics on the microbiome throughout development and alternative approaches for therapeutic modulation. *Genome Med.* **2016**, *8*, 39. [[CrossRef](#)] [[PubMed](#)]
2. Hollis, A.; Ahmed, Z. The path of least resistance: Paying for antibiotics in non-human uses. *Health Policy* **2014**, *118*, 264–270. [[CrossRef](#)] [[PubMed](#)]
3. Khalifa, S.A.M.; Shedid, E.S.; Saied, E.M.; Jassbi, A.R.; Jamebozorgi, F.H.; Rateb, M.E.; Du, M.; Abdel-Daim, M.M.; Kai, G.-Y.; Al-Hammady, M.A.M.; et al. Cyanobacteria—From the Oceans to the Potential Biotechnological and Biomedical Applications. *Mar. Drugs* **2021**, *19*, 241. [[CrossRef](#)]
4. Koch-Edelmann, S.; Banhart, S.; Saied, E.M.; Rose, L.; Aeberhard, L.; Laue, M.; Doellinger, J.; Arenz, C.; Heuer, D. The cellular ceramide transport protein CERT promotes Chlamydia psittaci infection and controls bacterial sphingolipid uptake. *Cell. Microbiol.* **2017**, *19*, e12752. [[CrossRef](#)] [[PubMed](#)]
5. Saied, E.M.; Banhart, S.; Burkle, S.E.; Heuer, D.; Arenz, C. A series of ceramide analogs modified at the 1-position with potent activity against the intracellular growth of Chlamydia trachomatis. *Future Med. Chem.* **2015**, *7*, 1971–1980. [[CrossRef](#)]
6. Banhart, S.; Saied, E.M.; Martini, A.; Koch, S.; Aeberhard, L.; Madela, K.; Arenz, C.; Heuer, D. Improved plaque assay identifies a novel anti-Chlamydia ceramide derivative with altered intracellular localization. *Antimicrob. Agents Chemother.* **2014**, *58*, 5537–5546. [[CrossRef](#)]
7. de Been, M.; van Schaik, W.; Cheng, L.; Corander, J.; Willems, R.J. Recent recombination events in the core genome are associated with adaptive evolution in *Enterococcus faecium*. *Genome Biol. Evol.* **2013**, *5*, 1524–1535. [[CrossRef](#)]
8. Johnson, A.P. The pathogenicity of enterococci. *J. Antimicrob. Chemother.* **1994**, *33*, 1083–1089. [[CrossRef](#)]
9. Weng, P.L.; Hamat, R.A.; Kqueen, Y.; Zainol, N.; Aziz, M.N.; Shamsudin, M.N. Vancomycin-resistant *Enterococcus faecium* of multi-locus sequence type 18 in Malaysia. *Med. J. Malays.* **2012**, *67*, 639–640.
10. Chen, C.; Sun, J.; Guo, Y.; Lin, D.; Guo, Q.; Hu, F.; Zhu, D.; Xu, X.; Wang, M. High prevalence of vanM in vancomycin-resistant *Enterococcus faecium* isolates from Shanghai, China. *Antimicrob. Agents Chemother.* **2015**, *59*, 7795–7798. [[CrossRef](#)]
11. Franz, C.M.; Huch, M.; Abriouel, H.; Holzapfel, W.; Gálvez, A. Enterococci as probiotics and their implications in food safety. *Int. J. Food Microbiol.* **2011**, *151*, 125–140. [[CrossRef](#)] [[PubMed](#)]
12. Brueggemann, A.B.; Pai, R.; Crook, D.W.; Beall, B. Vaccine escape recombinants emerge after pneumococcal vaccination in the United States. *PLoS Pathog.* **2007**, *3*, e168. [[CrossRef](#)] [[PubMed](#)]
13. Vazquez-Muñoz, R.; Meza-Villezcás, A.; Fournier, P.; Soria-Castro, E.; Juárez-Moreno, K.; Gallego-Hernández, A.; Bogdanchikova, N.; Vazquez-Duhalt, R.; Huerta-Saquero, A. Enhancement of antibiotics antimicrobial activity due to the silver nanoparticles impact on the cell membrane. *PLoS ONE* **2019**, *14*, e0224904. [[CrossRef](#)] [[PubMed](#)]
14. Edeoga, H.O.; Okwu, D.; Mbaebie, B. Phytochemical constituents of some Nigerian medicinal plants. *Afr. J. Biotechnol.* **2005**, *4*, 685–688. [[CrossRef](#)]
15. Meyer, M.S.; Joshipura, K.; Giovannucci, E.; Michaud, D.S. A review of the relationship between tooth loss, periodontal disease, and cancer. *Cancer Causes Control* **2008**, *19*, 895–907. [[CrossRef](#)]
16. Sohn, B.; Cohen, R. Processible optically transparent block copolymer films containing superparamagnetic iron oxide nanoclusters. *Chem. Mater.* **1997**, *9*, 264–269. [[CrossRef](#)]
17. Sharaf, M.; Sewid, A.H.; Hamouda, H.; Elharrif, M.G.; El-Demerdash, A.S.; Alharthi, A.; Hashim, N.; Hamad, A.A.; Selim, S.; Alkhalifah, D.H.M. Rhamnolipid-Coated Iron Oxide Nanoparticles as a Novel Multitarget Candidate against Major Foodborne *E. coli* Serotypes and Methicillin-Resistant *S. aureus*. *Microbiol. Spectr.* **2022**, *10*, e00250-22. [[CrossRef](#)]
18. Salata, O.V. Applications of nanoparticles in biology and medicine. *J. Nanobiotechnol.* **2004**, *2*, 3. [[CrossRef](#)]
19. Boss, A.; Bishop, K.S.; Marlow, G.; Barnett, M.P.; Ferguson, L.R. Evidence to support the anti-cancer effect of olive leaf extract and future directions. *Nutrients* **2016**, *8*, 513. [[CrossRef](#)]
20. Hassen, I.; Casabianca, H.; Hosni, K. Biological activities of the natural antioxidant oleuropein: Exceeding the expectation—A mini-review. *J. Funct. Foods* **2015**, *18*, 926–940. [[CrossRef](#)]
21. Lins, P.G.; Pugine, S.M.P.; Scatolini, A.M.; de Melo, M.P. In vitro antioxidant activity of olive leaf extract (*Olea europaea* L.) and its protective effect on oxidative damage in human erythrocytes. *Heliyon* **2018**, *4*, e00805. [[CrossRef](#)] [[PubMed](#)]
22. Acar-Tek, N.; Ağagündüz, D. Olive leaf (*Olea europaea* L. folium): Potential effects on Glycemia and Lipidemia. *Ann. Nutr. Metab.* **2020**, *76*, 10–15. [[CrossRef](#)] [[PubMed](#)]
23. El, S.N.; Karakaya, S. Olive tree (*Olea europaea*) leaves: Potential beneficial effects on human health. *Nutr. Rev.* **2009**, *67*, 632–638. [[CrossRef](#)] [[PubMed](#)]
24. Sulaiman, G.M.; Tawfeeq, A.T.; Jaaffer, M.D. Biogenic synthesis of copper oxide nanoparticles using *Olea europaea* leaf extract and evaluation of their toxicity activities: An in vivo and in vitro study. *Biotechnol. Prog.* **2018**, *34*, 218–230. [[CrossRef](#)]
25. Mary, M.G.A. Green synthesis of copper nanoparticles using *eclipta prostrata* leaves extract and their impact on seed germination and seedling growth of sorghum vulgare. *Galaxy Int. Interdiscip. Res. J.* **2021**, *9*, 168–186.
26. Alshawwa, S.Z.; Mohammed, E.J.; Hashim, N.; Sharaf, M.; Selim, S.; Alhuthali, H.M.; Alzahrani, H.A.; Mekky, A.E.; Elharrif, M.G. In Situ Biosynthesis of Reduced Alpha Hematite ( $\alpha$ -Fe<sub>2</sub>O<sub>3</sub>) Nanoparticles by *Stevia rebaudiana* L. Leaf Extract: Insights into Antioxidant, Antimicrobial, and Anticancer Properties. *Antibiotics* **2022**, *11*, 1252. [[CrossRef](#)]

27. Hou, Y.; Kovács, N.; Xu, H.; Sun, C.; Erni, R.; Gálvez-Vázquez, M.d.; Rieder, A.; Hu, H.; Kong, Y.; Liu, M. Limitations of identical location SEM as a method of degradation studies on surfactant capped nanoparticle electrocatalysts. *J. Catal.* **2021**, *394*, 58–66. [[CrossRef](#)]
28. Dipankar, C.; Murugan, S. The green synthesis, characterization and evaluation of the biological activities of silver nanoparticles synthesized from Iresine herbstii leaf aqueous extracts. *Colloids Surf. B Biointerfaces* **2012**, *98*, 112–119. [[CrossRef](#)]
29. Selim, M.S.; Hamouda, H.; Hao, Z.; Shabana, S.; Chen, X. Design of  $\gamma$ -AlOOH,  $\gamma$ -MnOOH, and  $\alpha$ -Mn<sub>2</sub>O<sub>3</sub> nanorods as advanced antibacterial active agents. *Dalton Trans.* **2020**, *49*, 8601–8613. [[CrossRef](#)]
30. Gaber, A.; Refat, M.S.; Belal, A.A.M.; El-Deen, I.M.; Hassan, N.; Zakaria, R.; Alhomrani, M.; Alamri, A.S.; Alsanie, W.F.; Saied, E.M. New Mononuclear and Binuclear Cu(II), Co(II), Ni(II), and Zn(II) Thiosemicarbazone Complexes with Potential Biological Activity: Antimicrobial and Molecular Docking Study. *Molecules* **2021**, *26*, 2288. [[CrossRef](#)]
31. Wang, Y.; Wu, Y.; Quadri, F.; Prox, J.D.; Guo, L. Cytotoxicity of ZnO nanowire arrays on excitable cells. *Nanomaterials* **2017**, *7*, 80. [[CrossRef](#)] [[PubMed](#)]
32. Berridge, M.V.; Tan, A.S. Characterization of the cellular reduction of 3-(4,5-dimethylthiazol-2-yl)-2,5-diphenyltetrazolium bromide (MTT): Subcellular localization, substrate dependence, and involvement of mitochondrial electron transport in MTT reduction. *Arch. Biochem. Biophys.* **1993**, *303*, 474–482. [[CrossRef](#)] [[PubMed](#)]
33. Gaber, A.; Alsanie, W.F.; Kumar, D.N.; Refat, M.S.; Saied, E.M. Novel Papaverine Metal Complexes with Potential Anticancer Activities. *Molecules* **2020**, *25*, 5447. [[CrossRef](#)] [[PubMed](#)]
34. Abdel-Wahab, B.A.; El-Kareem, H.F.A.; Alzamami, A.; Fahmy, C.A.; Elesawy, B.H.; Mahmoud, M.M.; Ghareeb, A.; el Askary, A.; Nahas, H.H.A.; Attallah, N.G.M.; et al. Novel Exopolysaccharide from Marine Bacillus subtilis with Broad Potential Biological Activities: Insights into Antioxidant, Anti-Inflammatory, Cytotoxicity, and Anti-Alzheimer Activity. *Metabolites* **2022**, *12*, 715. [[CrossRef](#)] [[PubMed](#)]
35. Kim, S.; Chen, J.; Cheng, T.; Gindulyte, A.; He, J.; He, S.; Li, Q.; Shoemaker, B.A.; Thiessen, P.A.; Yu, B.; et al. PubChem 2019 update: Improved access to chemical data. *Nucleic Acids Res.* **2019**, *47*, D1102–D1109. [[CrossRef](#)] [[PubMed](#)]
36. Fong, Y.H.; Wong, H.C.; Yuen, M.H.; Lau, P.H.; Chen, Y.W.; Wong, K.B. Structure of UreG/UreF/UreH complex reveals how urease accessory proteins facilitate maturation of Helicobacter pylori urease. *PLoS Biol.* **2013**, *11*, e1001678. [[CrossRef](#)] [[PubMed](#)]
37. Trott, O.; Olson, A.J. AutoDock Vina: Improving the speed and accuracy of docking with a new scoring function, efficient optimization, and multithreading. *J. Comput. Chem.* **2010**, *31*, 455–461. [[CrossRef](#)]
38. Alameen, A.A.; Abdalla, M.; Alshibl, H.M.; AlOthman, M.R.; Alkhulaifi, M.M.; Mirgany, T.O.; Elsayim, R. In-silico studies of glutathione peroxidase4 activators as candidate for multiple sclerosis management. *J. Saudi Chem. Soc.* **2022**, *26*, 101554. [[CrossRef](#)]
39. Healey, R.D.; Saied, E.M.; Cong, X.; Karsai, G.; Gabellier, L.; Saint-Paul, J.; del Nero, E.; Jeannot, S.; Drapeau, M.; Fontanel, S.; et al. Discovery and Mechanism of Action of Small Molecule Inhibitors of Ceramidases. *Angew. Chem. Int. Ed. Engl.* **2022**, *61*, e202109967. [[CrossRef](#)]
40. Khirallah, S.M.; Ramadan, H.M.M.; Shawky, A.; Qahl, S.H.; Baty, R.S.; Alqadri, N.; Alsuhaibani, A.M.; Jaremko, M.; Emwas, A.H.; Saied, E.M. Development of Novel 1,3-Disubstituted-2-Thiohydantoin Analogues with Potent Anti-Inflammatory Activity; In Vitro and In Silico Assessments. *Molecules* **2022**, *27*, 6271. [[CrossRef](#)]
41. Salem, M.G.; El-Maaty, D.M.A.; El-Deen, Y.I.M.; Elesawy, B.H.; Askary, A.E.; Saleh, A.; Saied, E.M.; Behery, M.E. Novel 1,3-Thiazole Analogues with Potent Activity against Breast Cancer: A Design, Synthesis, In Vitro, and In Silico Study. *Molecules* **2022**, *27*, 4898. [[CrossRef](#)] [[PubMed](#)]
42. Saied, E.M.; El-Maradny, Y.A.; Osman, A.A.; Darwish, A.M.G.; Nahas, H.H.A.; Niedbała, G.; Piekutowska, M.; Abdel-Rahman, M.A.; Balbool, B.A.; Abdel-Azeem, A.M. A Comprehensive Review about the Molecular Structure of Severe Acute Respiratory Syndrome Coronavirus 2 (SARS-CoV-2): Insights into Natural Products against COVID-19. *Pharmaceutics* **2021**, *13*, 1759. [[CrossRef](#)] [[PubMed](#)]
43. Mohamed, D.I.; El-Waseef, D.A.E.A.; Nabih, E.S.; El-Kharashi, O.A.; El-Kareem, H.F.A.; Nahas, H.H.A.; Abdel-Wahab, B.A.; Helmy, Y.A.; Alshawwa, S.Z.; Saied, E.M. Acetylsalicylic Acid Suppresses Alcoholism-Induced Cognitive Impairment Associated with Atorvastatin Intake by Targeting Cerebral miRNA155 and NLRP3: In Vivo, and In Silico Study. *Pharmaceutics* **2022**, *14*, 529. [[CrossRef](#)] [[PubMed](#)]
44. el Azab, I.H.; Saied, E.M.; Osman, A.A.; Mehana, A.E.; Saad, H.A.; Elkanzi, N.A. Novel N-bridged pyrazole-1-carbothioamides with potential antiproliferative activity: Design, synthesis, in vitro and in silico studies. *Future Med. Chem.* **2021**, *13*, 1743–1766. [[CrossRef](#)] [[PubMed](#)]
45. Samaha, D.; Hamdo, H.H.; Cong, X.; Schumacher, F.; Banhart, S.; Aglar, O.; Moller, H.M.; Heuer, D.; Kleuser, B.; Saied, E.M.; et al. Liposomal FRET Assay Identifies Potent Drug-Like Inhibitors of the Ceramide Transport Protein (CERT). *Chemistry* **2020**, *26*, 16616–16621. [[CrossRef](#)] [[PubMed](#)]
46. Daina, A.; Michielin, O.; Zoete, V. SwissADME: A free web tool to evaluate pharmacokinetics, drug-likeness and medicinal chemistry friendliness of small molecules. *Sci. Rep.* **2017**, *7*, 42717. [[CrossRef](#)]
47. Biovia, D.S. *Discovery Studio Modeling Environment, Release, 2017*; Dassault Systèmes: San Diego, CA, USA, 2017.
48. DeLano, W.L. *The PyMOL Molecular Graphics System*; Delano Scientific: San Carlos, CA, USA, 2002.

49. Sharaf, M.; Arif, M.; Hamouda, H.I.; Khan, S.; Abdalla, M.; Shabana, S.; Rozan, H.E.; Khan, T.U.; Chi, Z.; Liu, C. Preparation, urease inhibition mechanisms, and anti-Helicobacter pylori activities of hesperetin-7-rhamnoglucoside. *Curr. Res. Microb. Sci.* **2022**, *3*, 100103. [[CrossRef](#)]
50. Laskowski, R.A. PDBsum new things. *Nucleic Acids Res.* **2009**, *37*, D355–D359. [[CrossRef](#)]
51. Mou, K.; Abdalla, M.; Wei, D.Q.; Khan, M.T.; Lodhi, M.S.; Darwish, D.B.; Sharaf, M.; Tu, X. Emerging mutations in envelope protein of SARS-CoV-2 and their effect on thermodynamic properties. *Inform. Med. Unlocked* **2021**, *25*, 100675. [[CrossRef](#)]
52. Abraham, M.J.; Murtola, T.; Schulz, R.; Páll, S.; Smith, J.C.; Hess, B.; Lindahl, E. GROMACS: High performance molecular simulations through multi-level parallelism from laptops to supercomputers. *SoftwareX* **2015**, *1*, 19–25. [[CrossRef](#)]
53. Mark, P.; Nilsson, L. Structure and dynamics of the TIP3P, SPC, and SPC/E water models at 298 K. *J. Phys. Chem. A* **2001**, *105*, 9954–9960. [[CrossRef](#)]
54. Mohamed, D.I.; Ezzat, S.F.; Elayat, W.M.; El-Kharashi, O.A.; El-Kareem, H.F.A.; Nahas, H.H.A.; Abdel-Wahab, B.A.; Alshawwa, S.Z.; Saleh, A.; Helmy, Y.A.; et al. Hepatoprotective Role of Carvedilol against Ischemic Hepatitis Associated with Acute Heart Failure via Targeting miRNA-17 and Mitochondrial Dynamics-Related Proteins: An In Vivo and In Silico Study. *Pharmaceuticals* **2022**, *15*, 832. [[CrossRef](#)] [[PubMed](#)]
55. Mohamed, D.I.; Abou-Bakr, D.A.; Ezzat, S.F.; El-Kareem, H.F.A.; Nahas, H.H.A.; Saad, H.A.; Mehana, A.E.; Saied, E.M. Vitamin D3 Prevents the Deleterious Effects of Testicular Torsion on Testis by Targeting miRNA-145 and ADAM17: In Silico and In Vivo Study. *Pharmaceuticals* **2021**, *14*, 1222. [[CrossRef](#)] [[PubMed](#)]
56. Maqbool, Q.; Nazar, M.; Maqbool, A.; Pervez, M.T.; Jabeen, N.; Hussain, T.; Franklin, G. CuO and CeO<sub>2</sub> nanostructures green synthesized using olive leaf extract inhibits the growth of highly virulent multidrug resistant bacteria. *Front. Pharmacol.* **2018**, *9*, 987. [[CrossRef](#)]
57. Lim, A.; Subhan, N.; Jazayeri, J.; John, G.; Vanniasinkam, T.; Obied, H. Plant phenols as antibiotic boosters In vitro interaction of olive leaf phenols with ampicillin. *Phytother Res.* **2016**, *30*, 503–509. [[CrossRef](#)]
58. Maqbool, Q.; Nazar, M.; Naz, S.; Hussain, T.; Jabeen, N.; Kausar, R.; Anwaar, S.; Abbas, F.; Jan, T. Antimicrobial potential of green synthesized CeO<sub>2</sub> nanoparticles from *Olea europaea* leaf extract. *Int. J. Nanomed.* **2016**, *11*, 5015. [[CrossRef](#)]
59. Aziz, W.J.; Abid, M.A.; Hussein, E.H. Biosynthesis of CuO nanoparticles and synergistic antibacterial activity using mint leaf extract. *Mater. Technol.* **2020**, *35*, 447–451. [[CrossRef](#)]
60. Mahmoud, A.E.D.; Al-Qahtani, K.M.; Alflaij, S.O.; Al-Qahtani, S.F.; Alsamhan, F.A. Green copper oxide nanoparticles for lead, nickel, and cadmium removal from contaminated water. *Sci. Rep.* **2021**, *11*, 12547. [[CrossRef](#)]
61. Khalil, M.M.; Ismail, E.H.; El-Magdoub, F. Biosynthesis of Au nanoparticles using olive leaf extract: 1st nano updates. *Arab. J. Chem.* **2012**, *5*, 431–437. [[CrossRef](#)]
62. Zayyoun, N.; Bahmad, L.; Laânbab, L.; Jaber, B. The effect of pH on the synthesis of stable Cu<sub>2</sub>O/CuO nanoparticles by sol–gel method in a glycolic medium. *Appl. Phys. A* **2016**, *122*, 488. [[CrossRef](#)]
63. Maqbool, Q. Green-synthesised cerium oxide nanostructures (CeO<sub>2</sub>-NS) show excellent biocompatibility for phyto-cultures as compared to silver nanostructures (Ag-NS). *RSC Adv.* **2017**, *7*, 56575–56585. [[CrossRef](#)]
64. Siddiqui, H.; Parra, M.R.; Qureshi, M.; Malik, M.; Haque, F.Z. Studies of structural, optical, and electrical properties associated with defects in sodium-doped copper oxide (CuO/Na) nanostructures. *J. Mater. Sci.* **2018**, *53*, 8826–8843. [[CrossRef](#)]
65. Padil, V.V.T.; Černík, M. Green synthesis of copper oxide nanoparticles using gum karaya as a biotemplate and their antibacterial application. *Int. J. Nanomed.* **2013**, *8*, 889–898.
66. Adhikari, T.; Dube, G.; Kundu, S.; Patra, A. *Impact of Copper Oxide Nanoparticles on Growth of Different Bacterial Species, Energy and Environment*; Springer: Berlin/Heidelberg, Germany, 2018; pp. 47–55.
67. Yrken, Z. Minimum inhibitory concentration values and problematic disk break points of tigecycline against vancomycin and/or high-level aminoglycoside-resistant enterococci. *Alex. J. Med.* **2019**, *52*, 125–129.
68. Maalej, A.; Bouallagui, Z.; Hadrich, F.; Isoda, H.; Sayadi, S. Assessment of *Olea europaea* L. fruit extracts: Phytochemical characterization and anticancer pathway investigation. *Biomed. Pharmacother.* **2017**, *90*, 179–186. [[CrossRef](#)] [[PubMed](#)]
69. Withers, P.J.; van Dijk, K.C.; Neset, T.-S.S.; Nesme, T.; Oenema, O.; Rubæk, G.H.; Schoumans, O.F.; Smit, B.; Pellerin, S. Stewardship to tackle global phosphorus inefficiency: The case of Europe. *Ambio* **2015**, *44*, 193–206. [[CrossRef](#)] [[PubMed](#)]
70. Wang, L.; Hu, C.; Shao, L. The antimicrobial activity of nanoparticles: Present situation and prospects for the future. *Int. J. Nanomed.* **2017**, *12*, 1227. [[CrossRef](#)]
71. Wang, S.; Cazelles, R.; Liao, W.-C.; Vázquez-González, M.; Zoabi, A.; Abu-Reziq, R.; Willner, I. Mimicking horseradish peroxidase and NADH peroxidase by heterogeneous Cu<sup>2+</sup>-modified graphene oxide nanoparticles. *Nano Lett.* **2017**, *17*, 2043–2048. [[CrossRef](#)] [[PubMed](#)]
72. Li, Y.; Niu, J.; Shang, E.; Crittenden, J.C. Influence of dissolved organic matter on photogenerated reactive oxygen species and metal-oxide nanoparticle toxicity. *Water Res.* **2016**, *98*, 9–18. [[CrossRef](#)]
73. Kung, M.-L.; Tai, M.-H.; Lin, P.-Y.; Wu, D.-C.; Wu, W.-J.; Yeh, B.-W.; Hung, H.-S.; Kuo, C.-H.; Chen, Y.-W.; Hsieh, S.-L. Silver decorated copper oxide (Ag@CuO) nanocomposite enhances ROS-mediated bacterial architecture collapse. *Colloids Surf. B Biointerfaces* **2017**, *155*, 399–407. [[CrossRef](#)]
74. Kelly, K.L.; Coronado, E.; Zhao, L.L.; Schatz, G.C. *The Optical Properties of Metal Nanoparticles: The Influence of Size, Shape, and Dielectric Environment*; ACS Publications: Washington, DC, USA, 2003; pp. 668–677.

75. Alishah, H.; Pourseyedi, S.; Ebrahimipour, S.Y.; Mahani, S.E.; Rafiei, N. Green synthesis of starch-mediated CuO nanoparticles: Preparation, characterization, antimicrobial activities and in vitro MTT assay against MCF-7 cell line. *Rend. Lincei* **2017**, *28*, 65–71. [[CrossRef](#)]
76. Jinu, U.; Gomathi, M.; Saiqa, I.; Geetha, N.; Benelli, G.; Venkatachalam, P. Green engineered biomolecule-capped silver and copper nanohybrids using *Prosopis cineraria* leaf extract: Enhanced antibacterial activity against microbial pathogens of public health relevance and cytotoxicity on human breast cancer cells (MCF-7). *Microb. Pathog.* **2017**, *105*, 86–95. [[CrossRef](#)] [[PubMed](#)]
77. Sharma, P.; Goyal, D.; Baranwal, M.; Chudasama, B. ROS-induced cytotoxicity of colloidal copper nanoparticles in MCF-7 human breast cancer cell line: An in vitro study. *J. Nanopart. Res.* **2020**, *22*, 244. [[CrossRef](#)]
78. Biresaw, S.S.; Taneja, P. Copper nanoparticles green synthesis and characterization as anticancer potential in breast cancer cells (MCF7) derived from *Prunus nepalensis* phytochemicals. *Mater. Today Proc.* **2022**, *49*, 3501–3509. [[CrossRef](#)]
79. Fu, X. Oxidative stress induced by CuO nanoparticles (CuO NPs) to human hepatocarcinoma (HepG2) cells. *J. Cancer Ther.* **2015**, *6*, 889. [[CrossRef](#)]
80. Devipriya, D.; Roopan, S.M. *Cissus quadrangularis* mediated ecofriendly synthesis of copper oxide nanoparticles and its antifungal studies against *Aspergillus niger*, *Aspergillus flavus*. *Mater. Sci. Eng. C* **2017**, *80*, 38–44. [[CrossRef](#)]
81. Zhang, S.; Wang, Y.; Song, H.; Lu, J.; Yuan, Z.; Guo, J. Copper nanoparticles and copper ions promote horizontal transfer of plasmid-mediated multi-antibiotic resistance genes across bacterial genera. *Environ. Int.* **2019**, *129*, 478–487. [[CrossRef](#)]
82. Abbas, S.; Nasreen, S.; Haroon, A.; Ashraf, M.A. Synthesis of silver and copper nanoparticles from plants and application as adsorbents for naphthalene decontamination. *Saudi J. Biol. Sci.* **2020**, *27*, 1016–1023. [[CrossRef](#)]
83. Delatorre, P.; Silva-Filho, J.C.; Rocha, B.A.M.; Santi-Gadelha, T.; da Nóbrega, R.B.; Gadelha, C.A.A.; Nascimento, K.S.D.; Nagano, C.S.; Sampaio, A.H.; Cavada, B.S. Interactions between indole-3-acetic acid (IAA) with a lectin from *Canavalia maritima* seeds reveal a new function for lectins in plant physiology. *Biochimie* **2013**, *95*, 1697–1703. [[CrossRef](#)]
84. Shetty, K.N.; Latha, V.L.; Rao, R.N.; Nadimpalli, S.K.; Suguna, K. Affinity of a galactose-specific legume lectin from *Dolichos lablab* to adenine revealed by X-ray crystallography. *IUBMB Life* **2013**, *65*, 633–644. [[CrossRef](#)]
85. Rocha, B.A.; Teixeira, C.S.; Silva-Filho, J.C.; Nóbrega, R.B.; Alencar, D.B.; Nascimento, K.S.; Freire, V.N.; Gottfried, C.J.; Nagano, C.S.; Sampaio, A.H. Structural basis of ConM binding with resveratrol, an anti-inflammatory and antioxidant polyphenol. *Int. J. Biol. Macromol.* **2015**, *72*, 1136–1142. [[CrossRef](#)] [[PubMed](#)]